analytical chemistry

Article

pubs.acs.org/ac

Numerical Simulation of the Diffusion Processes in Nanoelectrode Arrays Using an Axial Neighbor Symmetry Approximation

Ana Sol Peinetti,[†] Rodrigo S. Gilardoni,[†] Martín Mizrahi,[‡] Felix G. Requejo,[‡] Graciela A. González,*[,†] and Fernando Battaglini*[,†]

[†]INQUIMAE,Departamento de Química Inorgánica, Analítica y Química Física, Facultad de Ciencias Exactas y Naturales, Universidad de Buenos Aires, Ciudad Universitaria, Pabellón 2, C1428EHA Buenos Aires, Argentina

[‡]Instituto de Investigaciones Físicoquímicas Teóricas y Aplicadas, INIFTA (CONICET y Dto. Química, Fac. Cs Ex, UNLP), 1900 La Plata, Argentina

Supporting Information

ABSTRACT: Nanoelectrode arrays have introduced a complete new battery of devices with fascinating electrocatalytic, sensitivity, and selectivity properties. To understand and predict the electrochemical response of these arrays, a theoretical framework is needed, with cyclic voltammetry, a well-fitted experimental technique to understand the undergoing diffusion and kinetics processes in necessary. Previous works describing microelectrode arrays have exploited the interelectrode distance to simulate its behavior as the summation of individual electrodes. This approach becomes limited when the size of the electrodes decreases to the nanometer scale due to their strong radial effect with the consequent overlapping of the diffusional fields. In this work, we present a computational model able to simulate the electrochemical behavior of arrays working either as the summation of individual electrodes or being affected by the overlapping of the diffusional fields without previous considerations. Our computational model relays in dividing a regular electrode array in cells. In each of them, there is a central electrode surrounded by neighbor electrodes; these neighbor electrodes are transformed in a ring maintaining the same active electrode area than the summation of the closest neighbor electrodes. Using this axial neighbor symmetry approximation, the problem acquires a cylindrical symmetry, being applicable to any diffusion pattern. The model is validated against micro- and nanoelectrode arrays showing its ability to predict their behavior and therefore to be used as a designing tool.

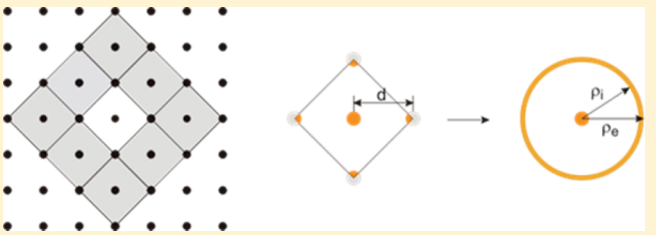

Microelectrode arrays have brought considerable attention to fundamental and technological research due to their ability to improve signal-to-noise ratio in analytical applications and facilitate kinetics studies.[1−6] More recently, the reduction of the electrode dimensions to nanometers not only enhances these features but also present interesting electrocatalytic effects,[7,8] high sensitivity,[9] and selectivity.[10]

Photolithography and electron beam lithography are the most popular techniques to build these arrays;[3,7,11−15] allowing the last one to achieve electrode diameters up to 50 nm.[12] Lithography is based on the application of an insulator layer onto a conductive substrate and, by either UV light or an electron beam, a pattern is created and later developed, generating pores. In the underneath of these pores, the conductive substrate works as micro- or nanoelectrodes.

Since the work of Menom and Martin,[16] a bottom-up approach, avoiding lithography, has also been used.[13,16−21] For example, Fontaine et al. constructed by sol−gel route nanoelectrode arrays constituted of nanoperforations of 16 nm in diameter leading to a platinum substrate and protected by an inorganic matrix made of crystalline zirconia.[20] Another example has been recently provided by using atomic layer deposition of insulating alumina on conductive carbon films masked by micrometer diameter polystyrene spheres, further removed by sonication, leaving in this way the carbon exposed as micro- and nanoelectrode arrays in the underneath surface.[21] Following this approach, another strategy can be taken inverting the construction sequence, generating first the porous structure and then growing the conductive material.[22,23] In line with this reasoning, we have generated gold nanoparticles (AuNPs) by electrochemical reduction inside porous alumina where the interfacial electron transfer is limited to the gold surface. This system presents several advantages: pores are easily built, with a good control of height and diameter; moreover, electrodes of different metals can be created with less than 3 nm diameter.[8] Finally, we were able to modify AuNPs with small molecule-binding aptamers inside the insulating pore, allowing discriminating small conformational changes in its surface.[10]

To understand and predict the electrochemical response of these arrays a theoretical framework is needed, with cyclic voltammetry a well-fitted experimental technique to understand

Received: January 5, 2016
Accepted: April 17, 2016

DOI: 10.1021/acs.analchem.6b00039
Anal. Chem. XXXX, XXX, XXX−XXX

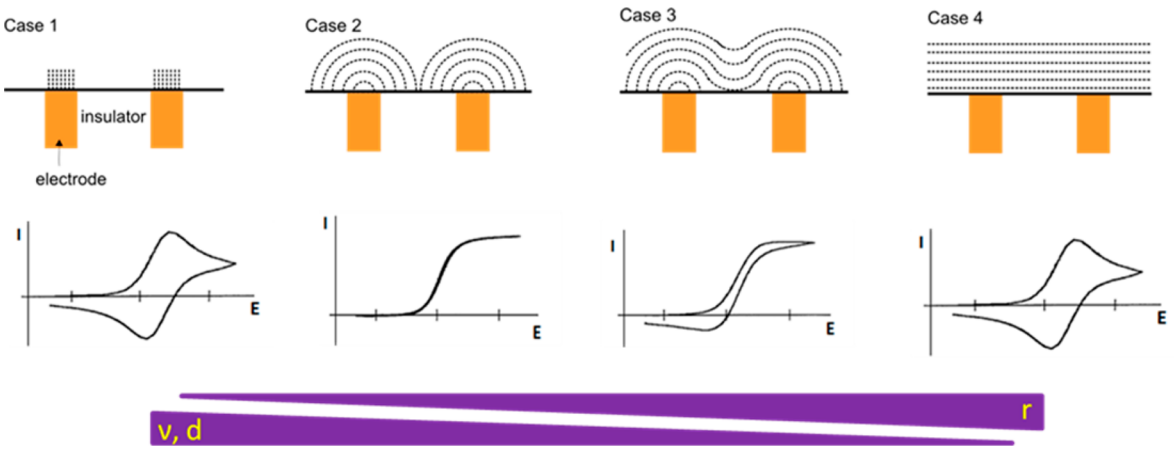

Figure 1. Scheme of the possible diffusion profiles in a micro- or nanoelectrode array and their corresponding cyclic voltammograms. The bars at the bottom indicate the trend behavior as a function of the electrode radius (r), the interelectrode distance (d), and scan rate (ν). As the parameter increases, the bar's width increases.

the undergoing diffusion and kinetics processes; however, a simple analytical description is not applicable and, instead, several groups have already presented interesting computational descriptions for these systems.[3,4,24,25]

The current response for an electrode array in a voltammetry experiment can be assigned mainly to three factors: scan rate, electrode radius, and interelectrode distance, which in turn produce four different diffusional patterns illustrated in Figure 1. Cases 1 and 4 can be described by planar diffusion; therefore, it is reduced to a 1-dimensional problem. Case 2 can be treated as individual microelectrodes, while Case 3 is more complex since the overlapping of the adjacent diffusional layers forbids its treatment as independent microelectrodes but, on the other hand, the diffusional fields are not so heavily overlapped to be considered equivalent to a linear diffusion case (Case 4). Therefore, of the four cases, it is the most challenging to deal. This situation has been already observed in nanoelectrode arrays,[21,26] since as the electrode surface decreases, the participation of the radial diffusion increases. This process scales with the inverse of the electrode radius,[27] reaching a relevant weight at the nanometer scale.

Compton and co-workers[3,4] developed a two-dimensional simulation method, by identifying the key factors involved when a cyclic voltammetry is applied on these arrays. The 2-dimensional method is based on the diffusion domain approximation (DDA).[24] The DDA model considers a regular distribution of N electrodes, for instance a square or a hexagonal lattice, where the electrodes have a circular area of radius r and are separated by a distance d; the area covered can be divided in N individual unit cells each centered on an electrode. Figure 2 shows a scheme summarizing the geometrical parameters and the unit cells. Note that the length of the unit cell is equal to the interelectrode distance. This division of the system simplifies the simulation process to only one unit cell, as far the diffusion fields do not overlap (Case 2 in Figure 1); therefore, to obtain the response of the array, the behavior of one cell is multiplied by the N elements of the array. In this way, a unit cell with cylindrical symmetry is built based on its area, which reduces the three-dimensional problem to a two-dimensional one.

The model considers a zero net flux across the walls of the diffusion domain, a valid condition depending on the scan rate and the size of the electrode. Therefore, there is a need to

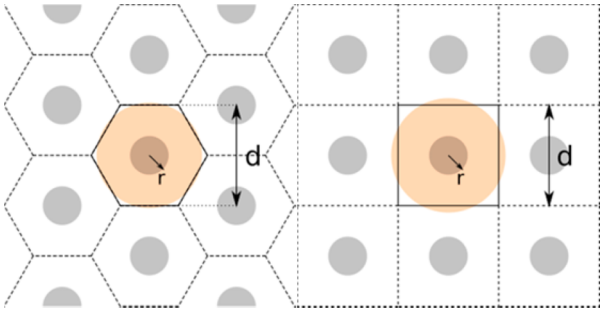

Figure 2. Unit cell definition by the DDA model. Left, hexagonal array; right, square array. The circle establishes the transformed unit cell as it is defined in ref 4.

define a critical distance between the electrode center and the unit cell limit, where the error due to the overlapping of the diffusion layers is still negligible. This distance is practically a half of the interelectrode distance and can be applied above a certain scan rate. This scan rate was arbitrarily chosen, which results in a 2.5% decrease in peak (or limiting) current compared to the case where the microelectrodes in the array are infinitely separated. This fact limits its application to the whole range of scan rates and, as the electrode radius decreases, this limitation becomes more important.

Amatore and co-workers[5] have shown that the application of the quasi-conformal mapping transforms the simulation area from the real complex geometry onto a square unit and removes singularities at corners of the initial computational domain in the real space. This strategy allows enhancing the efficiency of the numerical calculation, the accuracy to simulate arrays of recessed microelectrodes and evaluate the dependence of these processes on the main geometrical parameters. However, also this model considers wells with walls perpendicular to its edges and no crossing fluxes among them, remaining the limitation in the cases where there is diffusion overlapping.

The models previously described are useful to explain the behavior of arrays with electrodes bearing a radius in the order of micrometers. In these cases, a proposed condition for observing independent behavior of the active sites, and therefore avoiding a overlapping effect is $d/r \geq 12$; a condition

DOI: 10.1021/acs.analchem.6b00039
Anal. Chem. XXXX, XXX, XXX−XXX

that cannot be held when the electrodes of the array downsizes to the nanometer scale.

In this work, we present a different approach taking into account the possible overlapping of the diffusional field of each electrode with its closest neighbors. Our computational model relays in dividing a regular electrode array in cells (Figure 3, left). In each of these cells, there is a central electrode surrounded by neighbor electrodes; these neighbor electrodes are transformed in a ring (Figure 3, right) maintaining the same active electrode area than the summation of the closest neighbor electrodes. Using this axial neighbor symmetry approximation (ANSA), the problem acquires a cylindrical symmetry, which takes into account also the consumption of its neighbors, being applicable to any diffusion pattern. On one hand, this concept preserves the simplicity of the 2D computational treatment, and on the other, it improves the previous models, where their application depends on the combination of the interelectrode distance, the electrode radius, the scan rate, and the diffusion coefficient involved in the problem, rationalized by the work of Guo and Linder without a quantitative solution.[6] The model presented here can also be applicable to either coplanar or recessed electrodes. The new model was validated with experimental data for hexagonal and square arrays containing electrodes with radius from 1.3 nm to 10 μm covering the transition between the different cases shown in Figure 1.

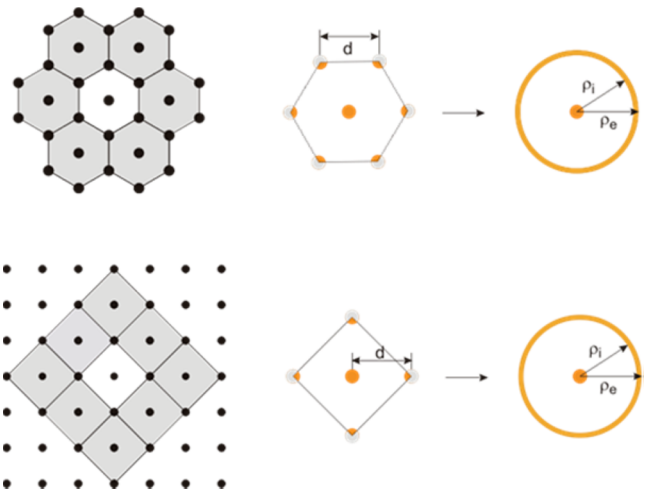

Figure 3. Left, unit cell definition by the ANSA model; top, hexagonal array; bottom, square array. Right, transformation of a unit cell in the array into a system with axial symmetry; top, transformation for a hexagonal array considering the closest neighbors; bottom, transformation for a square array considering the closest neighbors.

MATHEMATICAL MODEL

The Axial Neighbor Symmetry Approximation (ANSA) is applicable to an array of either recessed or coplanar electrodes with a radius r, separated by a distance d.

The model defines a cell that compromises a central electrode and their closest neighbors (Figure 3, left). Then, the neighbor electrodes are evaluated considering how each of them is shared among the neighbor cells (gray shaded in Figure 3, left). Therefore, the effective area (A_{ef}) for the first neighbors can be calculated in a general way as

$$A_{ef} = \frac{\theta}{2} n r^2 \quad (1)$$

where, θ is the angle sweeping the surface of a neighbor electrode allocated in the studied cell (white cell in Figure 3, left), n is the number of closest neighbor electrodes, and r the radius of the electrode. For the hexagonal array, θ is $2\pi/3$ radians (120°) and for the square array is $\pi/2$ radians (90°).

The position of the ring is established by considering that its internal radius (ρ_i) is equal to

$$\rho_i = d - r \quad (2)$$

and its area is defined by

$$A_{ef} = \pi(\rho_e^2 - \rho_i^2) \quad (3)$$

considering eqs 1 and 3, the external radius (ρ_e) is defined by

$$\rho_e = \sqrt{\rho_i^2 + \frac{A_{ef}}{\pi}} = \sqrt{\rho_i^2 + \frac{\theta}{2\pi} n r^2} \quad (4)$$

therefore, for an square array:

$$\rho_e = \sqrt{\rho_i^2 + r^2} \quad (5)$$

and for an hexagonal array

$$\rho_e = \sqrt{\rho_i^2 + 2r^2} \quad (6)$$

This experimental system was modeled solving Poisson and Nernst–Plank without electroneutrality equations[28] using a finite-element software (Comsol Multiphysics 3.4) and the flux of electroactive species at the electrode is given by the Buttler Volmer equation, to obtain the voltammetric response and the concentration profiles, as previous works.[9,28−30] The mass transport is controlled entirely by diffusion. The space dimension was set to axial 2D symmetry to reduce the amount of calculation. In the Supporting Information, the proposed setup and boundary conditions are given in detail. Simulations based on the Diffusion Domain Approximation (DDA) were carried out using Comsol Multiphysics following conditions given in ref 4.

EXPERIMENTAL SECTION

Materials. All reagents were analytical grade. Tetrachloroauric acid ($HAuCl_4 \cdot 3H_2O$) was provided from Aldrich. Water (18 MΩ cm^{-1}) was provided by Millipore Simplicity equipment.

Array C: Construction and Electrochemical Characterization. Working electrodes (4 mm^2) were prepared from aluminum 1145 (99.5%). Surface pretreatment was carried out degreasing the surface in an ultrasonic bath with acetone, followed by electropolishing in a 5:1 ethanol–$HClO_4$ solution (v/v) at 18 V for 1 min. The cleaned surface was immediately exposed to an acid electrolyte (15% H_2SO_4) at room temperature (15 V, 1 min), using a lead plate as counter electrode in front of the working electrode. Once the electrode was anodized, it was left 5 min in the acid electrolyte and then rinsed with Milli-Q water. Pore size and depth were characterized by scanning electron microscopy.

Gold electrodeposition was carried out using a 10 mM $HAuCl_4$ solution at pH 4.0. Anodized aluminum and a gold plate were used as working and counter electrodes, respectively. Gold electrodeposition was performed in three steps: (i) metal deposition at −3 mA cm^{-2} for 8 ms; (ii) application of 3 mA

DOI: 10.1021/acs.analchem.6b00039
Anal. Chem. XXXX, XXX, XXX−XXX

Table 1. Arrays Tested

array	material	electrode radius/μm	interelectrode distance/μm	pore depth/μm	electrodes in the array	ref
A	Pt	10.0 ± 0.2	100 ± 1	1	210	4
B	Au	5.0 ± 0.2	100 ± 1	1	72	4
C	Au	$(1.3 \pm 0.3) \times 10^{-3}$	$(35 \pm 4) \times 10^{-3}$	1	2.6×10^{9}	this work
D	C	$(9.7 \pm 0.2) \times 10^{-2}$	1.54	0.010	2.41×10^{7}	21
E	Au	$(3.4 \pm 0.2) \times 10^{-2}$	0.110	0.010	8.5×10^{9}	26

cm^{-2} for 2 ms; (iii) no current is applied during 500 ms, to recover the ion concentration in the pores by diffusion from the solution. In total, 1000 cycles were performed.

Cyclic voltammetries of Array C were carried out in a solution of 50 mM $K_4[Fe(CN)_6]$ in 50 mM HEPES buffer, pH 7.0.

FESEM Micrographs. Micrographs were taken with a field emission scanning electron microscope (FESEM) Zeiss DSM 982 Gemini at the Advanced Center for Microscopies (CMA, Universidad de Buenos Aires). Pores size and interpore distance distributions were calculated using ImageJ software. Figure S1 (Supporting Information) shows the aspect of Array C.

X-ray Techniques (Array C). Nanoparticle size was estimated from the coordination numbers determined by extended X-ray absorption fine structure (EXAFS). Au L_3-edge EXAFS spectra were measured at room temperature in fluorescence mode at the XAFS2 beamline at the Laboratorio Nacional de Luz Síncrotron (LNLS, Campinas, Brazil). An ionization chamber was used to detect the incident flux and a 15-element germanium solid state detector was used to sense the fluorescence signal from the sample. Data were processed using ATHENA with the AUTOBK background removal algorithm.[31] The spectra were calibrated using a metallic film of gold. The EXAFS oscillations $\chi(k)$ were extracted from the experimental data with standard procedures using the Athena program.[32] The k^2 weighted $\chi(k)$ data, to enhance the oscillations at higher k, were Fourier transformed. The Fourier transformation was calculated using the Hanning filtering function. EXAFS modeling was carried out using the ARTEMIS program which is part of the IFFEFIT package.[31,32] The k-range was set from 2.5 to 11.5 Å^{-1}. The passive reduction factor S_0^2 value was restrained to 0.9. This value was obtained from fitting a standard foil of gold by constraining the coordination number in this compound of known crystal structure. Details of the average diameter particle calculation are given in Supporting Information.

RESULTS AND DISCUSSION

Table 1 presents the characteristics of the electrode arrays used in this work to validate the ANSA model. The experimental data correspond to results already published and our own. The work of Davies et al.[4] results very useful since it allows to test the new model with an impressive number of experimental results, reporting also complete information regarding the parameters needed to simulate de cyclic voltammetries and allowing to compare DDA and ANSA models with the experimental data.

In the cited work, two regular arrays of microelectrodes were studied, their characteristics are reproduced in Table 1; the rest of parameters needed for the simulation were taken from the same publication and they are reproduced in the Supporting Information.

Array A was used to study the response of a 1 mM $[Ru(NH_3)_6]^{3+}$, 0.1 M KCl solution to cyclic voltammetry at different scan rates, ranging from 0.01 to 2 V s^{-1}. As the voltammetries are plotted and the peak currents tabulated, it is possible to make a comparison between the two models and the experimental results. Figure 4(top) shows an example of the

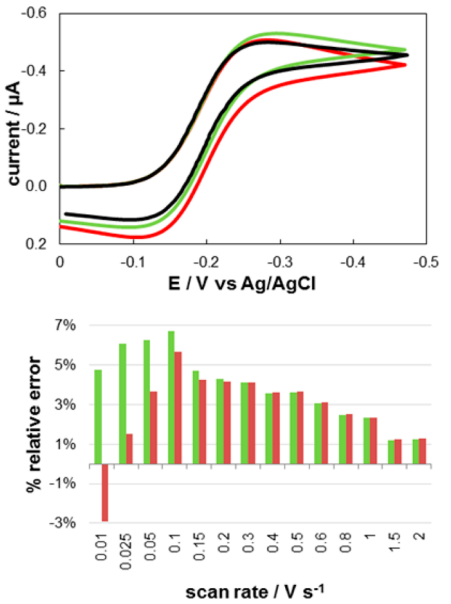

Figure 4. (Top) Cyclic voltammetry of a 1 mM $[Ru(NH_3)_6]^{3+}$ + 0.1 M KCl solution at 25 mV s^{-1} for Array A: black line, experimental data; green line, simulated data with DDA model; red line, simulated data with ANSA model. (Bottom) Percentage relative error for the prediction of the maximum current at different scan rates, DDA model in green, ANSA model in red. Experimental data taken from ref 4.

simulated voltammetries compared to the experimental result; while, Figure 4(bottom) plots the percentage relative error obtained in the simulation of the maximum currents respect to the experimental results at different scan rates.

The other example presented by Davies et al. is a smaller array (Array B) exposed to a solution of 1 mM ferrocyanide plus 0.1 M KCl. Cyclic voltammetries in the range from 0.01 to 0.15 V s^{-1} were carried out. In this case, as the electrode radius is smaller and the interelectrode distance the same, the consumption of the probe decreases and therefore the overlap of the diffusion fields is negligible even at low scan rates, with errors smaller than 3% for both models (see Figure S4 in Supporting Information).

It should be pointed out that both arrays were designed to comply with case 2; therefore, the DDA model fits very well and it is useful to show that the model presented in this work is also able to fit these cases. Furthermore, the ANSA model presents smaller relative errors at scan rates below 0.2 V s^{-1} in the case of Array A (Figure 4, bottom), since it takes into

DOI: 10.1021/acs.analchem.6b00039
Anal. Chem. XXXX, XXX, XXX−XXX

account the overlap of the diffusional field. On the other hand, over 0.2 V s^{-1} both models produces the same result, since the array behaves as the summation of the independent microelectrodes. Finally, both models are applicable when the array can be considered as "infinite", i.e., when the radial diffusion at its edges can be neglected.[5] This is the case for all the arrays presented in this work.

Another aspect to take into account in this type of arrays is the size of the individual electrodes, as technology allows smaller diameters, the radial component effect of each electrode is more relevant. This situation can be exemplified by an array of nanoelectrodes recently produced by our group that consists in the formation of gold nanoparticles in a porous alumina array. As it is known, anodized aluminum oxide (AAO) represents a simple route to the construction of arrays with hexagonal 2D order and have used for the synthesis of metal nanowires;[33] while our group, taking a different approach, was able to synthesize nanoparticles below 2 nm radius.[8,10] Briefly, our method consisted of (I) the creation of an oxide nanoporous structure, (II) the chemical etching of the oxide barrier layer by sulfuric acid, and (III) pulsed electrodeposition of the metal in the pores. The thinning of the oxide layer and the density current used in the electrodeposition process (see the Experimental Section) are key steps in the nanoparticle generation. In this work, the synthesis of gold nanoparticles from a $[AuCl_4]^-$ solution yields nanoparticles of 1.3 ± 0.3 nm of radius. The size of the generated AuNPs were determined in situ by extended X-ray absorption fine structure (EXAFS) at the AuL3-edge. This X-ray absorption technique provides information on the local environment of Au atoms, i.e., the number, type, and distances of Au neighborhood without altering the geometry of the sample used for the electrochemical reaction. Details on radius determination are given in the Supporting Information.

f5 Figure 5 (top) shows the experimental result of a cyclic voltammetry for a 50 mM ferrocyanide solution at 100 mV s^{-1}, compared to the predicted values obtained using the ANSA and DDA models, while Figure 5 (bottom) shows the percentage relative difference between the maximum current predicted by the models and the experimental results. In this case the difference between the models is greater, being ANSA the most accurate. It is noteworthy to point out that for both models the relative differences are higher than the previous cases. This can be attributed to several reasons, experimental ones, as bigger uncertainties in the array features when it is produced by bottom-up procedures compared to photolithography (see Table 1) and due to the limitations of the model. While a model with diffusional control as the presented here is a good approach to the study of these recessed systems, it is noteworthy that this conventional treatment (electroneutrality and exclusive diffusion-controlled transport) may become inaccurate to electrodes with less than 5 nm radius due to enhanced effects of the diffuse double layer on the interfacial charge transport and electron transfer processes. A more accurate simulation of mass transport in this type of nanoelectrodes requires explicit consideration of the double layer and its effects[34−37]

To show the versatility of the model, other two arrays were tested with electrode radii of 97 and 34 nm, arrays D and E, respectively, which do not exhibit the limitations of the previous example. The main characteristics of these arrays are presented in Table 1. Array D corresponds to a nanoelectrode hexagonal array produced in alumina, where the electroactive

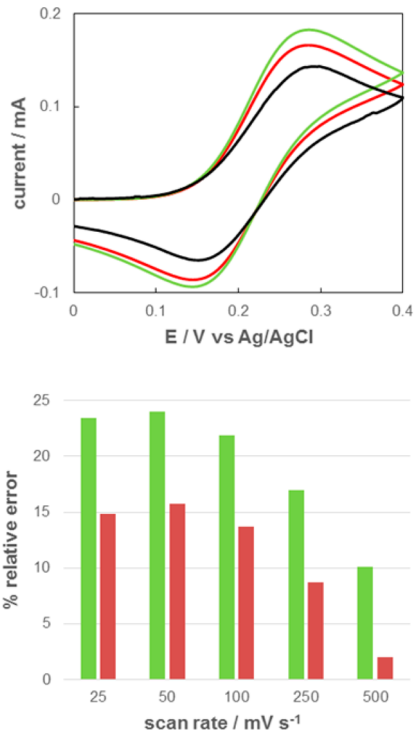

Figure 5. (top) Cyclic voltammetry of 50 mM $K_4[Fe(CN)_6]$ in 50 mM HEPES buffer, pH 7.0 at 100 mV s^{-1} for Array C: black line, experimental data; green line, simulated data with DDA model; red line, simulated data with ANSA model. (bottom) Relative percentage error in maximum current prediction at different scan rates, DDA model in green, ANSA model in red.

material is carbon obtained by a pyrolitic proccess.[21] The interesting features of this case is the fact that the electrode radius is in the submicrometer scale and the ratio between the interelectrode distance and the electrode radius is 16. Through impedance experiments, the authors concluded that this array can approach a behavior of parallel independent nanoelectrodes in a cyclic voltammetry experiment only if the scan rate is higher than 6 V s^{-1}. While at very slow scan rates, 1 mV s^{-1}, the authors report a closer behavior to Case 4. Therefore, we tested our model against their experimental results, covering scan rates between 0.01 and 1 V s^{-1}, to follow the transition of the diffusional regime from practically linear diffusion (Case 4, low scan rates) to parallel independent electrodes.

For an array working under conditions of Case 4, the peak current can be calculated considering the array as an electrode with a partially blocked surface; this causes an apparent decrease of the heterogeneous rate transfer constant which is proportional to the fractional electrochemical active area.[16,20,24] Therefore, one option to consider is comparing the experimental values to those predicted as the case of infinite plane electrode (Case 4, Figure 1) with a fractional active area (0.0144) and acting as a quasireversible system.[38] On the other extreme, the behavior as parallel independent electrodes (Case 2) can be predicted by

$$i_{ind} = \frac{4nFDC^{o}r}{\left(\frac{4h}{\pi r}\right) + 1} \quad (7)$$

where C^o is the bulk concentration of the probe, r is the electrode radius, h is the pore depth, and the rest of the symbols have the usual meanings.[39] Taking into account the

DOI: 10.1021/acs.analchem.6b00039
Anal. Chem. XXXX, XXX, XXX−XXX

number of nanoelectrodes, the expected current for this array would be 398.8 μA.

Table 2 presents the peak currents at different scan rates predicted by considering the array as an electrode with a

Table 2. Comparison of the Peak Current Predicted against Experimental Values for Array D (Currents in μA)

scan rate/mV s^{-1}	quasi-reversible	ANSA	experimental (ref21)
10	28	22	23
50	61	43	46
100	84	57	62
500	178	95	94
1000	247	113	100

quasirevesible behavior (column 2), predicted by ANSA (column 3) and the experimental values (column 4). In this case, the simulation was carried out by calculating 4 cycles to achieve a stationary response similar to the observed in the experimental results. Figure 6 shows the fitting for a 100 mV s^{-1} cyclic voltammetry.

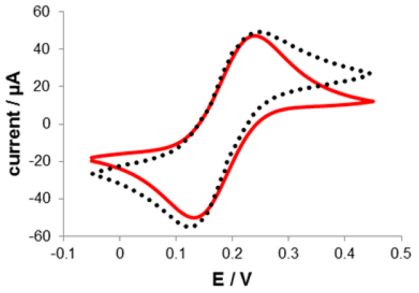

Figure 6. Cyclic voltammetry of a 1 mM ferrocenemethanol solution at 100 mV s^{-1} for Array D: black dotted line, experimental data; red line, simulated data with ANSA model. Experimental data taken from ref 21

Returning to Table 2, it can be observed that at the 10 mV s^{-1} scan rate, the difference between the two calculated currents and the experimental value is small. However, as the scan rate increases, neither of the two analytical models (Case 2, 398.8 μA, and Case 4, tabulated) can explain the experimental results, while ANSA is able to predict the peak currents with a relative error less than 10% until 500 mV s^{-1}. At higher scan rates, the experimental values are affected by an uncompensated resistance, already observable at 0.1 V s^{-1} (Figure 6). See the slope in the initial scan for the experimental voltammogram compared to the simulated one, and this behavior is more striking as the scan rate increases.

Finally, the experimental data of another nanoelectrode array constructed by a bottom-up approach was simulated using our model (Array E). In this case, the data belongs to a work published by Lantiat et al.,[26] and the array is formed by electrodes of 34 nm radius at an interelectrode distance of 110 nm. In this case, the electrochemical behavior observed at the scan rates used in the work represent a clear transition between Cases 3 and 4.

Table 3 shows the small differences between the experimental results and those predicted taking into account an electrode array operating under overlap conditions. As it was explained for the previous case, the array behaves like a electrode with a partially blocked surface. Therefore, the experimental values have to be compared with those predicted

Table 3. Comparison of the Peak Current Predicted against Experimental Values for Array E (Currents in mA)

scan rate/mV s^{-1}	quasi-reversible	ANSA	experimental (ref26)
10	0.096	0.070	0.070
50	0.203	0.148	0.152
200	0.388	0.281	0.322
500	0.594	0.431	0.482

considering the case of infinite plane electrode (Case 4, Figure 1) with a fractional active area, in this case 0.33, and acting as a quasireversible system.[38] The differences with the experimental values show a narrow range (23−35%) compared to the previous example, where at high scan rates differences are over 75%. Considering the experimental uncertainties, the behavior of this array can be considered very close to case 4. In the same table, it can be observed that ANSA is able to predict the peak currents with less than 12% error for all the cases.

It is also important to highlight the difference in electrode radius between the arrays constructed by photolitography and the generated by electrodeposition in alumina, the ratio between the radii of arrays B and C is 3800. This impressive reduction in size has an important effect in the diffusional profile surrounding each electrode, manifested in the shape of the voltammogram, that can be considered as an example of case 3.

As it was previously stated, the electrode radius plays a key role in the formation of the diffusional field. Let us consider that the efficiency to produce current by each electrode in an array is given by how close its experimental value is from the current produced by an isolated nano- or microelectrode. This can be easy determined by predicting the current of an individual recessed electrode using eq 7 (i_{ind}), and the current predicted by the ANSA model for a single electrode in the array ($i_{s,ANSA}$). The ratio between $i_{s,ANSA}/i_{ind}$ at different electrode sizes and the interelectrode distances will give us an idea of their effect on the current efficiency.

Figure 7 compares the current ratio obtained for electrodes of 5 nm and 5 μm radius in arrays of recessed electrodes (1 μm) at different interelectrode distances considering a cyclic voltammetry for a solution similar to the one used in Array C at 50 mV s^{-1}. The interelectrode distance is defined in a relative scale where the unit is the electrode radius for each case. An important point to be raised is the radial diffusion effect in each

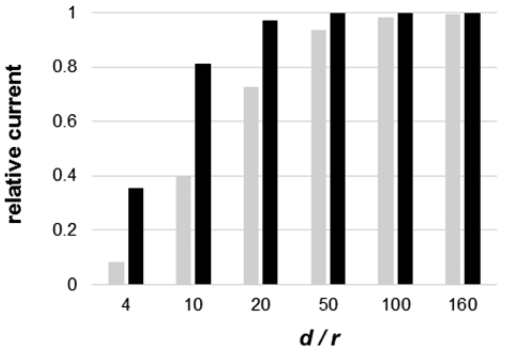

Figure 7. Relative current of an electrode in an array respect to an individual electrode for different interelectrode distances. Currents were obtained simulating cyclic voltammetries at 50 mV s^{-1}. In gray, results for a 5 nm radius electrode; in black, results for a 5 μm radius electrode. Pore depth: 1 μm.

DOI: 10.1021/acs.analchem.6b00039
Anal. Chem. XXXX, XXX, XXX−XXX

electrode; for the 5 μm electrode, in the time scale of the experiment shown in Figure 7, the current is mainly produced by the perpendicular flow of the probe to each individual electrode and the overlapping of diffusion fields can be neglected. On the other hand, for the 5 nm electrode, the radial flow represents an important contribution and the overlapping of the diffusional fields will be immediately noticeable. As it can be seen, at a separation of 20 times r the electrodes are not able to work as individual ones in the nanometer scale, while in the micrometer scale the difference is negligible; this effect is more dramatic as the interelectrode distance decreases, and the same tendency is observed when the pore depth decreases. These situations are commonly observed in many nanoelectrode arrays constructed by bottom-up procedures,[8,21,26] where the condition $d/r \geq 12$ for independent electrode behavior cannot be applied.

The proposed model allows changing the scan rates, interelectrode distance and the depth of the electrodes without restriction, making possible to analyze their different effects in the design of electrode arrays. Examples regarding these parameters are presented in the Supporting Information where the effect of scan rate (Figures S5) and pore depth (Figure S6) are presented.

CONCLUSIONS

In this work the simulation of cyclic voltammetry experiments with nano- and microelectrode arrays was carried out using a model where the closest neighbor electrodes were taken into account in the diffusion and electron transfer process undergone by an electroactive species. The model splits the array in cells formed by a central electrode plus its closest neighbors as a ring surrounding it. As the examples shown here, taken only the closest neighbors the model is able to match the experimental results of five arrays that cover different diffusion patterns (Figure 1). Also, this work represents an improvement in the treatment of the diffusion mass transport in recessed nano- and microelectrode arrays where the diffusional control can be verified.[34−37] The model is able to consider any case regardless of the time scale of the experiment, representing a valuable tool for the design of these type of arrays. Particularly, its application is well suited when the electrode achieves nanometer dimensions in systems constructed by a bottom-up approach, where the ratio between the interelectrode distance and electrode radius is more difficult to control.[8,21,26] The model is able to work with nanometer size electrodes (examples C, D, and E) where the overlapping of diffusional fields is important, even at interelectrode distances higher than 12 times the electrode radius, a distance generally proposed for observing independent behavior of the electrodes.[25] Finally, as the method works directly with real dimensions, it can be used by neophytes.

ASSOCIATED CONTENT

Supporting Information

The Supporting Information is available free of charge on the ACS Publications website at DOI: 10.1021/acs.analchem.6b00039.

Additional experimental information on Array C (Figures S1 and S2), numerical domain and boundary conditions (Figure S3), parameters used in the simulations, validation of Array B (Figure S4), and effect of the nanometric radius on the current response (Figures S5 and S6) (PDF)

AUTHOR INFORMATION

Corresponding Authors

*E-mail: graciela@qi.fcen.uba.ar.

*E-mail: battagli@qi.fcen.uba.ar. Fax: 54-11-45763341. Phone: 54-11-45763358.

Author Contributions

The manuscript was written through contributions of all authors. All authors have given approval to the final version of the manuscript.

Notes

The authors declare no competing financial interest.

ACKNOWLEDGMENTS

This work was financially supported by the following grants: ANPCyT PICT-2011-0406, UBACYT, XAFS1 beamline (LNLS, Brazil) Proposal 17189. M.M., G.A.G., F.G.R., and F.B. are CONICET members.

REFERENCES

(1) Ongaro, M.; Ugo, P. *Anal. Bioanal. Chem.* **2013**, *405*, 3715−3729.

(2) Zhu, F.; Yan, J.; Pang, S.; Zhou, Y.; Mao, B.; Oleinick, A.; Svir, I.; Amatore, C. *Anal. Chem.* **2014**, *86*, 3138−3145.

(3) Davies, T. J.; Compton, R. G. *J. Electroanal. Chem.* **2005**, *585*, 63−82.

(4) Davies, T. J.; Ward-Jones, S.; Banks, C. E.; del Campo, F. J.; Mas, R.; Muñoz, F. X.; Compton, R. G. *J. Electroanal. Chem.* **2005**, *585*, 51−62.

(5) Amatore, C.; Oleinick, A. I.; Svir, I. *Anal. Chem.* **2009**, *81*, 4397−4405.

(6) Guo, J.; Lindner, E. *Anal. Chem.* **2009**, *81*, 130−138.

(7) Fernandez, J. L.; Wijesinghe, M.; Zoski, C. G. *Anal. Chem.* **2015**, *87*, 1066−1074.

(8) Peinetti, A. S.; Herrera, S.; González, G. A.; Battaglini, F. *Chem. Commun.* **2013**, *49*, 11317−11319.

(9) Zhang, B.; Zhang, Y. H.; White, H. S. *Anal. Chem.* **2004**, *76*, 6229−6238.

(10) Peinetti, A. S.; Ceretti, H.; Mizrahi, M.; González, G. A.; Ramírez, S. A.; Requejo, F. G.; Montserrat, J. M.; Battaglini, F. *Nanoscale* **2015**, *7*, 7763−7769.

(11) Godino, N.; Borrise, X.; Muñoz, F. X.; del Campo, F. J.; Compton, R. G. *J. Phys. Chem. C* **2009**, *113*, 11119−11125.

(12) Ziaie, B.; Baldi, A.; Atashbar, M. Z. Introduction to Micro-/Nanofabrication. In *Springer Handbook of Nanotechnology*, 3rd ed.; Bhushan, B., Ed.; Springer-Verlag: Berlin, Heidelberg, Germany, 2010.

(13) Lanyon, Y. H.; De Marzi, G.; Watson, Y. E.; Quinn, A. J.; Gleeson, J. P.; Redmond, G.; Arrigan, D. W. M. *Anal. Chem.* **2007**, *79*, 3048−3055.

(14) Sandison, M. E.; Cooper, J. M. *Lab Chip* **2006**, *6*, 1020−1025.

(15) Moretto, L. M.; Tormen, M.; De Leo, M.; Carpentiero, A.; Ugo, P. *Nanotechnology* **2011**, *22*, 185305.

(16) Menon, V. P.; Martin, C. R. *Anal. Chem.* **1995**, *67*, 1920−1928.

(17) Baker, W. S.; Crooks, R. M. *J. Phys. Chem. B* **1998**, *102*, 10041−10046.

(18) De Leo, M.; Pereira, F. C.; Moretto, L. M.; Scopece, P.; Polizzi, S.; Ugo, P. *Chem. Mater.* **2007**, *19*, 5955−5964.

(19) Perera, D. M. N. T.; Ito, T. *Analyst* **2010**, *135*, 172−176.

(20) Fontaine, O.; Laberty-Robert, C.; Sanchez, C. *Langmuir* **2012**, *28*, 3650−3657.

(21) Duay, J.; Goran, J. M.; Stevenson, K. J. *Anal. Chem.* **2014**, *86*, 11528−11532.

(22) Nielsch, K.; Müller, F.; Li, A.-P.; Gösele, U. *Adv. Mater.* **2000**, *12*, 582−586.

DOI: 10.1021/acs.analchem.6b00039
Anal. Chem. XXXX, XXX, XXX−XXX

588 (23) Tian, M.; Xu, S.; Wang, J.; Kumar, N.; Wertz, E.; Li, Q.;
589 Campbell, P. M.; Chan, M.H. W.; Mallouk, T. E. *Nano Lett.* **2005**, *5*,
590 697−703.
591 (24) Amatore, C.; Saveant, J. M.; Tessier, D. *J. Electroanal. Chem.*
592 *Interfacial Electrochem.* **1983**, *147*, 39−51.
593 (25) Lee, H. J.; Beriet, C.; Ferrigno, R.; Girault, H. H. *J. Electroanal.*
594 *Chem.* **2001**, *502*, 138−145.
595 (26) Lantiat, D.; Vivier, V.; Laberty-Robert, C.; Grosso, D.; Sanchez,
596 C. *ChemPhysChem* **2010**, *11*, 1971−1977.
597 (27) Bard, A.; Faulkner, L.; *Electrochemical Methods*, 2nd ed.; Wiley:
598 New York, 2001; Chapter 5.
599 (28) Newman, J.; Thomas-Alyea, K.; *Electrochemical Systems*, 3rd ed.;
600 Wiley: New York, 2004; Chapter 11.
601 (29) Zhang, Y. H.; Zhang, B.; White, H. S. *J. Phys. Chem. B* **2006**,
602 *110*, 1768−1774.
603 (30) González, G.; Priano, G.; Günther, M.; Battaglini, F. *Sens.*
604 *Actuators, B* **2010**, *144*, 349−353.
605 (31) Ravel, B.; Newville, M. *J. Synchrotron Radiat.* **2005**, *12*, 537−
606 541.
607 (32) Newville, M. *J. Synchrotron Radiat.* **2001**, *8*, 322−324.
608 (33) Lee, W.; Park, S. J. *Chem. Rev.* **2014**, *114*, 7487−7556.
609 (34) Smith, C. P.; White, H. S. *Anal. Chem.* **1993**, *65*, 3343−3353.
610 (35) Sun, Y.; Liu, Y.; Liang, Z.; Xiong, L.; Wang, A.; Chen, S. *J. Phys.*
611 *Chem. C* **2009**, *113*, 9878−9883.
612 (36) Liu, Y.; He, R.; Zhang, Q.; Chen, S. *J. Phys. Chem. C* **2010**, *114*,
613 10812−10822.
614 (37) Dickinson, E. J. F.; Compton, R. J. *J. Phys. Chem. C* **2009**, *113*,
615 17585−17589.
616 (38) Bard, A.; Faulkner, L.; *Electrochemical Methods*, 2nd ed.; Wiley:
617 New York, 2001; Chapter 6.
618 (39) Bond, A. M.; Luscombe, D.; Oldham, K. B.; Zoski, C. G. *J.*
619 *Electroanal. Chem. Interfacial Electrochem.* **1988**, *249*, 1−14.

DOI: 10.1021/acs.analchem.6b00039
Anal. Chem. XXXX, XXX, XXX−XXX